

Probing Dark Photon Dark Matter with CTAO

Júlia G. Mamprim, Aion Viana and Vitor de Souza

Instituto de Física de São Carlos, Universidade de São Paulo, Av. Trabalhador São-carlense 400, São Carlos, Brasil

E-mail: juliagouveamamprim@usp.br, aion@ifsc.usp.br, vitor@ifsc.usp.br

Abstract. The dark photon is a new hypothetical gauge boson arising in extensions of the Standard Model, and constitutes a compelling dark matter candidate. As dark photon dark matter (DPDM), it can interact with electromagnetic fields via kinetic mixing, and the inelastic scattering process $\gamma\gamma' \rightarrow e^+e^-$ becomes kinematically allowed for gamma rays above a characteristic energy threshold. This interaction imprints unique spectral attenuation features at very-high-energies (VHE), offering an observational probe of DPDM models. Using the Cherenkov Telescope Array Observatory (CTAO) Instrument Response Functions (IRFs), we simulate observations of VHE sources and forecast novel sensitivities to the kinetic mixing parameter for the photon-dark photon scattering process. Our study focuses on three key astrophysical targets: the Crab Nebula and the blazars Markarian 421 and Markarian 501. Additionally, we investigate the impact of dark matter spikes around black holes on the upper limits. Our results demonstrate that CTAO can probe the DPDM parameter space down to a mixing parameter of $\varepsilon \sim 10^{-8}$ for masses around $m_{A'} \sim 10^{-1}$ eV through high-energy spectral attenuation, at a 95% confidence level.

Contents

1	Introduction	1
2	Photon-dark photon scattering	2
3	Dark matter density profiles	4
3.1	Navarro-Frenk-White	4
3.2	Dark matter spikes around black holes	5
4	Astrophysical sources	6
4.1	Crab Nebula	6
4.2	Mrk 421 and Mrk 501	6
5	CTAO simulated observations	9
5.1	Crab Nebula spectral simulations	10
5.2	Mrk 421 and Mrk 501 spectral simulations	11
6	Model fitting	13
6.1	Null Hypothesis H_0	13
6.2	Alternative Hypothesis H_1	14
6.3	Log-likelihood statistical test	14
7	Results	15
8	Conclusion	17

1 Introduction

Dark Matter (DM) constitutes approximately 27% of the total energy density of the Universe and dominates the matter content on cosmological scales [1, 2]. Its existence is firmly supported by a wealth of astrophysical and cosmological evidence, including galaxy rotation curves [3], cluster dynamics [4], the Cosmic Microwave Background (CMB) [5], and large-scale structure formation [6]. Despite this strong astrophysical evidence, the particle nature of DM remains unknown, with no confirmed signals from direct detection experiments (e.g., LUX [7], XENONnT [8], PandaX-4T [9]) or indirect searches (e.g., Fermi-LAT [10], H.E.S.S. [11], IceCube [12])(see e.g. [13] for a comprehensive summary of constraints across different channels).

Hidden sector extensions of the Standard Model have emerged as compelling frameworks to address the nature of dark matter. Among these models, one possibility involves the introduction of a new Abelian gauge boson, the dark photon γ' , associated with an additional $U(1)'$ symmetry [14, 15]. In this scenario, dark photons produced non-thermally

in the early Universe can account for all or a fraction of the dark matter content observed today [16, 17]. Through kinetic mixing with the SM photon, dark photon dark matter (DPDM) leads to observable effects, despite being otherwise extremely weakly coupled [18, 19].

A potential phenomenological signature of DPDM is its inelastic interaction with high-energy photons through the process $\gamma\gamma' \rightarrow e^+e^-$, which becomes kinematically allowed when the center-of-mass energy exceeds twice the electron mass. For dark photon masses in the eV range, this mechanism can lead to energy-dependent attenuation features in the spectra of VHE gamma-ray sources [20, 21]. Such spectral signatures may serve as probes of DPDM models in observations conducted by present and next-generation gamma-ray telescopes.

In this work, we use the most recent Cherenkov Telescope Array Observatory (CTAO) Instrument Response Functions (IRFs) to simulate observations of three well-known VHE sources: the Crab Nebula, and the blazars Markarian 421 and Markarian 501. We analyze the expected attenuation features in the gamma-ray spectra induced by the inelastic scattering process to derive constraints on the kinetic mixing parameter ε over a range of dark photon masses. Additionally, we examine how the presence of dark matter overdensities, or “spikes”, around supermassive black holes can enhance the predicted attenuation from blazars.

This paper is structured as follows. In Section 2, we summarize the theoretical framework of photon–dark photon scattering and present the relevant cross-section for this process. Section 3 discusses the dark matter density profiles adopted in our analysis, including standard Navarro–Frenk–White profiles and dark matter spikes around supermassive black holes. Section 4 provides an overview of the astrophysical sources considered (Crab Nebula, Mrk 421, and Mrk 501), highlighting their spectral energy distributions and the associated dark matter environments. Section 5 details the simulation procedure using CTAO IRFs and the modeling of the gamma-ray spectra for each source. In Section 6, we describe the statistical methodology used to fit the models and derive expected upper limits on the kinetic mixing parameter. Our results are presented in Section 7, followed by concluding remarks in Section 8.

2 Photon-dark photon scattering

The phenomenology of the massive dark photon is characterized by its interaction with Standard Model (SM) particles, as described by the Lagrangian [19]

$$\mathcal{L} \supset -\frac{e\varepsilon}{\sqrt{1-\varepsilon^2}} J_\mu A'^\mu \simeq -e\varepsilon J_\mu A'^\mu, \quad (2.1)$$

where A'^μ is the gauge field associated with the dark photon, ε is a dimensionless mixing parameter, e is the electromagnetic coupling constant, and J_μ represents the SM electromagnetic current.

The low-energy effective theory emerges when considering energy scales E satisfying the hierarchy $m_{A'} \lesssim E \ll m_f$, where m_f denotes the mass scale of hypothetical heavy fermions charged under both the Standard Model $U(1)_{\text{EM}}$ and the hidden $U(1)'$ gauge

groups, which mediate the interaction between the visible and dark sectors. In this regime, integrating out the heavy fermions yields the effective Lagrangian

$$\mathcal{L} \supset -\frac{1}{4}\mathcal{F}^{\mu\nu}\mathcal{F}_{\mu\nu} - \frac{\varepsilon}{2}\mathcal{F}^{\mu\nu}\mathcal{F}'_{\mu\nu} - \frac{1}{4}\mathcal{F}'^{\mu\nu}\mathcal{F}'_{\mu\nu}, \quad (2.2)$$

where $F_{\mu\nu}$ and $F'_{\mu\nu}$ are the field strength tensors for the SM photon and dark photon, respectively.

If the DP has a non-zero mass, the scattering process $\gamma\gamma' \rightarrow e^+e^-$ becomes kinematically accessible for gamma rays with energies above the threshold

$$E > E'_{\text{th}} = \frac{2m_e^2}{m_{A'}}, \quad (2.3)$$

where m_e is the mass of the electron and $m_{A'}$ is the mass of the dark photon. At leading order, the photon can undergo scattering with the two transversely polarized modes of the dark photon, mediated by its coupling to electrons through mixing with the QED photon. The corresponding scattering cross-section is [21]

$$\sigma_{A'} = \frac{8\pi\varepsilon^2\alpha^2}{3(s - m_{A'}^2)^3} \left[-\beta(s^2 + 4sm_e^2 + m_{A'}^4) + \ln\left(\frac{1+\beta}{1-\beta}\right) \times (s^2 + 4sm_e^2 + m_{A'}^4 - 4m_{A'}^2m_e^2 - 8m_e^4) \right], \quad (2.4)$$

with $\beta = \sqrt{1 - 4m_e^2/s}$ and $s = 2Em_{A'} + m_{A'}^2$. The dependence of the scattering cross section on the photon energy is shown in Figure 1.

This process can produce a detectable attenuation effect in the spectrum of VHE gamma ray sources. Assuming the dark photon constitutes all the dark matter in the Universe, the photon survival probability induced by the photon-dark photon scattering is

$$P_{\text{sur}} = e^{-\tau_{A'}}, \quad (2.5)$$

where $\tau_{A'}$ is the optical depth due to the DPDM scattering, expressed as the integral along the line of sight (LOS) of the DPDM number density $n_{A'} = \rho_{\text{DM}}/m_{A'}$

$$\tau_{A'} = \int_{\text{los}} n_{A'}\sigma_{A'}dl. \quad (2.6)$$

Note that the survival probability depends on the dark matter density profile ρ_{DM} , and this dependence varies with the location of the source and the properties of the intervening medium along the line of sight.

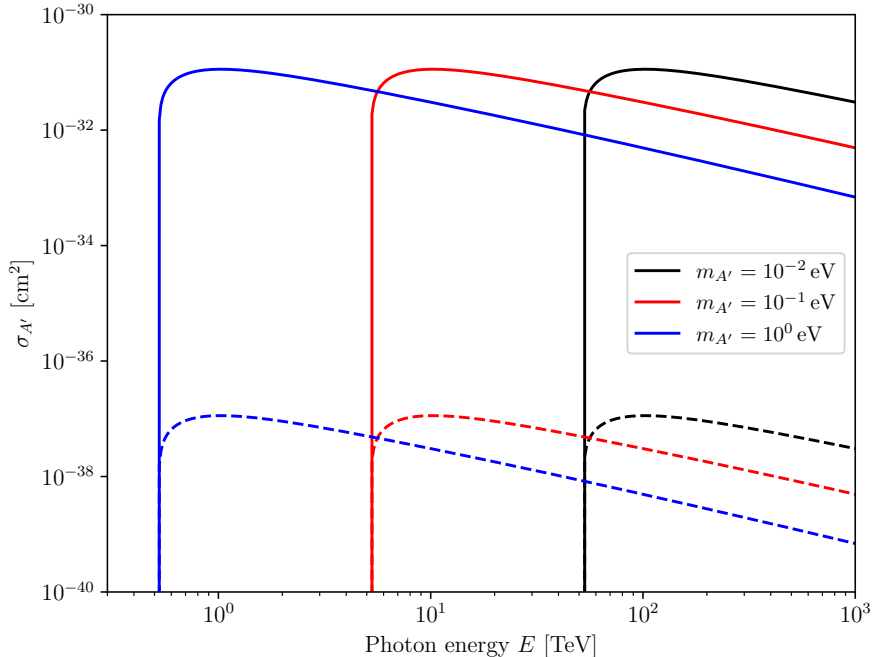


Figure 1. Photon–dark-photon scattering cross section $\sigma_{A'}$ as a function of the photon energy for representative dark-photon masses. Solid (dashed) lines correspond to $\varepsilon = 10^{-3}$ (10^{-6}).

3 Dark matter density profiles

The distribution of dark matter in galaxies and galaxy clusters is commonly described using spherically symmetric halo density profiles, $\rho_{\text{DM}}(r)$. These profiles can vary significantly depending on the morphology, mass, and formation history of the system. Therefore, for the different astrophysical sources considered in this study, distinct dark matter density profiles must be adopted to accurately represent the underlying dark matter distributions.

The Zhao [22] profile provides a unified framework for characterizing dark matter spherical halos through a power-law function

$$\rho_{\text{Zhao}}(r) = \rho_s \left(\frac{r}{r_s} \right)^{-\gamma} \left[1 + \left(\frac{r}{r_s} \right)^\alpha \right]^{(\gamma-\beta)/\alpha}, \quad (3.1)$$

where the characteristic density ρ_s and scale radius r_s set the overall normalization and size of the halo, respectively. The inner slope parameter γ governs the central cusp behavior ($\rho \propto r^{-\gamma}$), while β controls the outer slope ($\rho \propto r^{-\beta}$). The transition parameter α determines how sharply the profile changes between these regimes.

3.1 Navarro-Frenk-White

Emerging from N-body simulations of collisionless dark matter, the Navarro-Frenk-White (NFW) [23] profile represents a canonical halo density distribution of dark matter in

Λ CDM cosmology. It emerges by choosing $(\alpha, \beta, \gamma) = (1, 3, 1)$ in the Zhao profile (Eq. 3.1). Explicitly,

$$\rho_{\text{NFW}}(r) = \frac{\rho_s}{(r/r_s)(1+r/r_s)^2}. \quad (3.2)$$

For the Milky Way (MW), we assume $r_s = 14.46$ kpc and $\rho_s = 0.566$ GeV/cm³ [13], constrained by the local dark matter density $\rho_\odot = \rho(r_\odot) = 0.4$ GeV/cm³ [13].

3.2 Dark matter spikes around black holes

A further relevant consideration is the potential existence of dark matter spikes around black holes, which are localized density enhancements arising from the adiabatic growth of compact massive objects, such as supermassive black holes (SMBHs) [24]. These spikes could substantially enhance the expected signals in indirect dark matter detection searches.

An initial power-law dark matter density profile evolves into a spike profile [24, 25]

$$\rho_{\text{sp}}(r) = \rho_R g_\gamma(r) \left(\frac{R_{\text{sp}}}{r} \right)^{\gamma_{\text{sp}}}, \quad (3.3)$$

with the spike radius R_{sp} given by

$$R_{\text{sp}} = \alpha_\gamma r_s \left(\frac{M_{\text{BH}}}{\rho_s r_s^3} \right)^{1/(3-\gamma)}, \quad (3.4)$$

where $\gamma_{\text{sp}} = \frac{9-2\gamma}{4-\gamma}$ is the spike power-law index, and the factors α_γ and $g_\gamma(r)$ are obtained numerically. For typical values of $\gamma = 0.7-1.4$, we have $\alpha_\gamma \simeq 0.1$ and $g_\gamma(r) \simeq 1 - \frac{4R_S}{r}$ [24], where R_S is the Schwarzschild radius of the black hole. Furthermore, a normalization factor $\rho_R = \rho_0(R_{\text{sp}}/r_0)^{-\gamma}$ is needed in order to ensure continuity with the density profile outside the spike region. The spike profile is valid only for $4R_S \leq r \leq R_{\text{sp}}$, vanishing at smaller radii due to capture by the black hole. At radii $r > R_{\text{sp}}$, the dark matter distribution maintains its original power-law profile (e.g. NFW).

This spike profile only holds for non-annihilating dark matter or in scenarios where annihilation is negligible, such as the DPDM case we are considering. However, for dark matter models with substantial annihilation cross-sections, the central density saturates at an equilibrium value, leading to the formation of an inner core.

The spike normalization is determined under the constraint that the enclosed dark matter mass at radii relevant for black hole mass determinations (typically $\sim 10^5 R_S$ [26, 27]) does not exceed the uncertainty on the black hole mass ΔM_{BH} [28],

$$\int_{4R_S}^{10^5 R_S} 4\pi r^2 \rho_{\text{DM}} dr \lesssim \Delta M_{\text{BH}}. \quad (3.5)$$

4 Astrophysical sources

According to Eq. 2.3, photon–dark photon scattering becomes kinematically allowed at energies above 52 TeV for dark photon masses of $m_{A'} = 10^{-2}$ eV. This energy threshold establishes the minimum gamma-ray energies needed to probe the model, motivating the selection of astrophysical sources with significant emission in the TeV regime. In this section, we present the selected sources, outlining their overall characteristics, spectral properties and the associated dark matter density distributions considered in the analysis.

4.1 Crab Nebula

The Crab Nebula is a galactic source located in the Taurus constellation at a distance of approximately 2 kpc, and represents one of the most important and well-studied VHE sources in astrophysics [29]. This system originated from a supernova explosion observed in AD 1054 and consists of three primary components: the Crab Pulsar PSR B0531+21, the surrounding pulsar wind nebula and the expanding supernova remnant itself [29–31]. The Crab Nebula dominates as one of the brightest high-energy and very-high-energy sources in the sky. Its exceptional luminosity, coupled with remarkably stable emission properties, has established it as the standard candle for VHE astronomy and a natural laboratory for studying particle acceleration and non-thermal emission processes in extreme astrophysical environments.

The Crab Nebula spectral energy distribution reveals two distinct components: synchrotron emission from relativistic electrons in the nebula’s magnetic field dominates the lower energies ($\lesssim 1$ GeV), while inverse Compton (IC) scattering of ultrarelativistic electrons produces the high-energy peak [32–36]. Recent detections of PeV photons by LHAASO [37] have revitalized interest in hadronic contributions to the gamma-ray flux [38, 39], though leptonic processes remain dominant across most of the spectrum.

The nebula spectral energy distribution (SED) at VHE is typically modeled by a log-parabola function of the form

$$\frac{dN}{dE} = N_0 \left(\frac{E}{E_0} \right)^{-\alpha - \beta \log(E/E_0)}, \quad (4.1)$$

where $E_0 = 7$ TeV is the reference energy. In our simulations, we adopt the parameters as estimated by the analysis of HAWC observations [40]: $N_0 = (2.35 \pm 0.04) \times 10^{-13} \text{ TeV}^{-1} \text{ s}^{-1} \text{ cm}^{-2}$, $\alpha = 2.79 \pm 0.02$ and $\beta = 0.10 \pm 0.01$.

Since the Crab Nebula is a Galactic source, we model the surrounding dark matter distribution using the NFW profile (Eq. 3.2) with parameters consistent with the Milky Way halo. This profile is shown in Figure 2, and the corresponding LOS integral is computed based on the source’s location, as given in Table 1.

4.2 Mrk 421 and Mrk 501

Markarian 421 (Mrk 421) and Markarian 501 (Mrk 501) are two of the most extensively studied blazars in VHE gamma-ray astronomy. These objects are classified as BL

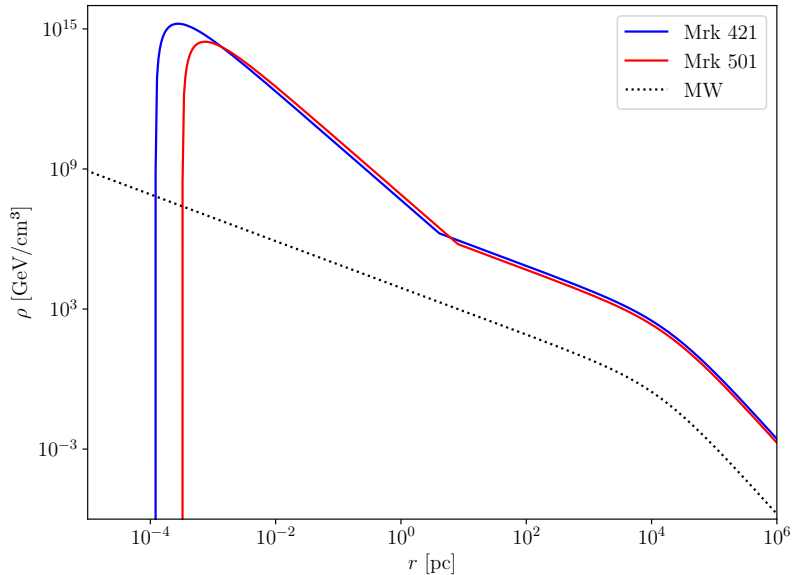


Figure 2. Radial dark matter density profiles for Mrk 421 (blue) and Mrk 501 (red) host galaxies, modeled with a dark matter spike (parameters in Table 2). The dotted black line shows the Milky Way’s NFW profile for comparison, normalized to the local density at r_{\odot} (black dotted line).

Lacertae-type blazars, a subclass of active galactic nuclei (AGN) characterized by featureless optical spectra and strong non-thermal emission. Their jets are aligned close to the observer’s line of sight, leading to significant relativistic boosting and making them prominent sources in the VHE regime [41–43].

Mrk 421, located in the constellation Ursa Major, was the first extragalactic object detected at TeV energies, discovered in 1992 by the Whipple Observatory [43]. Mrk 421 is known for its dramatic flaring episodes in the TeV band. In 2001 it exhibited a historic flare where the flux exceeded the Crab Nebula flux [44, 45].

Mrk 501, in the constellation Hercules, became the second confirmed TeV blazar after detection in 1996 by the Whipple collaboration [46]. During a major 1997 flare, its VHE flux exceeded that of the Crab Nebula, with its emission also being observed beyond 20 TeV [47].

Such events offer critical insights into particle acceleration and radiation mechanisms in AGN jets. Simultaneous multiwavelength campaigns on both sources, using instruments such as MAGIC, HAWC, HEGRA, VERITAS, H.E.S.S., and Fermi-LAT, have enabled modeling of their spectral energy distributions (SEDs) and testing of leptonic and hadronic models [45, 48–54].

The intrinsic energy spectra of Mrk 421 and Mrk 501 are well-described by an exponential cutoff power-law (ECPL) function

$$\frac{dN}{dE} = N_0 \left(\frac{E}{1 \text{ TeV}} \right)^{-\alpha} \exp \left(-\frac{E}{E_{\text{cut}}} \right), \quad (4.2)$$

where N_0 , α , and E_{cut} are the normalization, spectral index, and cutoff energy, respectively. Time-averaged observations of the TeV energy spectrum of Mrk 421, conducted by the HEGRA system of Cherenkov telescopes during the period of Nov. 2000 - May 2001 (totaling an observation time of 254.8 h), resulted in the best-fit parameters $N_0 = (11.4 \pm 0.3) \times 10^{-11} \text{ TeV}^{-1} \text{ s}^{-1} \text{ cm}^{-2}$, $\alpha = 2.19 \pm 0.02$ and $E_{\text{cut}} = 3.6 \text{ TeV}$ [45]. HEGRA has also monitored Mrk 501 in the TeV range during the several months of the source's outburst in 1997, and the time-averaged observations resulted in the best-fit parameters $N_0 = (10.8 \pm 0.2) \times 10^{-11} \text{ TeV}^{-1} \text{ s}^{-1} \text{ cm}^{-2}$, $\alpha = 1.92 \pm 0.03$ and $E_{\text{cut}} = 6.2 \pm 0.4 \text{ TeV}$ [55].

Strictly speaking, photons originating from the sources Mrk 421 and Mrk 501 propagate not only through their host galaxy environments but also traverse the intergalactic medium (IGM) and the Milky Way before reaching Earth. Consequently, the optical depth can be decomposed into three distinct components

$$\begin{aligned} \tau_{A'} &= \tau_{A',\text{host}} + \tau_{A',\text{IGM}} + \tau_{A',\text{MW}} \\ &= \int_{\text{los}} (\rho_{\text{DM,host}} + \rho_{\text{DM,IGM}} + \rho_{\text{DM,MW}}) \times (\sigma_{A'}/m_{A'}) dl. \end{aligned} \quad (4.3)$$

For the Milky Way's dark matter density distribution, we adopt the NFW profile (Eq. 3.2) with the standard Galactic parameterization described in Section 3. The intergalactic medium (IGM) contains a very low density of dark matter, which can be approximated as $\rho_{\text{DM,IGM}} = \Omega_{\text{DM}} \times \rho_c$. Here, $\Omega_{\text{DM}} \approx 0.26$ is the present-day dark matter density parameter, and $\rho_c \approx 8.64 \times 10^{-30} \text{ g cm}^{-3}$ is the critical density of the universe in the Λ CDM model [1].

For the host galaxies of the sources Mrk 421 and Mrk 501, we use a spike profile as described in Section 3, with a NFW profile adopted at radii $r > R_{\text{sp}}$. The scale density ρ_s and the spike radius R_{sp} are set by taking the upper bound in Eq. 3.5, while the scale radius is fixed as $r_s = 20 \text{ kpc}$, consistent with typical parameterizations for galaxies lacking well-constrained rotation curve measurements [56–59]. The parameters of both host galaxies are displayed in Table 2, and the corresponding DM density profiles are shown in Figure 2.

Source	R.A. (hh mm ss)	Dec (dd mm ss)	Distance
Crab	05 34 30.9	+22 00 44.5	2 kpc
Mrk 421	11 04 19	+38 11 41	$z = 0.031$
Mrk 501	16 53 52.2	+39 45 37	$z = 0.034$

Table 1. Distances and equatorial coordinates of the sources [60].

Source	γ	$\rho_s(\text{GeVcm}^{-3})$	$r_s(\text{kpc})$	$R_{\text{sp}}(\text{pc})$	$\log(M_{\text{BH}}/M_{\odot})$
Mrk 421	1	357.73	20	4.10	8.50 ± 0.18
Mrk 501	1	244.73	20	8.13	8.93 ± 0.21

Table 2. Parameters of Mrk 421 and Mrk 501 dark matter density profiles. The SMBH masses and their associated uncertainties were adopted from Ref. [61].

The VHE gamma-ray emissions are produced in compact regions situated relatively close to their central SMBHs, with radial distances that may vary in the broad range of $R_{\text{em}} \approx (4-10^4)R_S$ [51, 62–64]. The DM mass integrals along the line-of-sight for Mrk 421 and Mrk 501 host galaxies, considering four different emission regions R_{em} , are shown in Figure 3. The contributions of the MW halo and IGM to the total integrated DM mass are negligible when compared to the dominant host galaxy’s dark matter distribution, being smaller by a factor of $\sim 10^{-8}$ and $\sim 10^{-9}$ respectively.

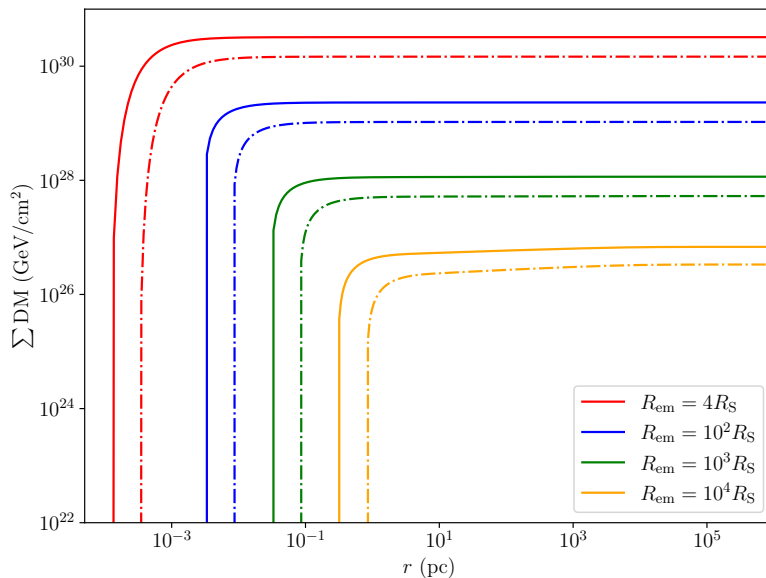


Figure 3. Line-of-sight (LOS) integrals of the dark matter mass for the host galaxies of Mrk 421 (solid lines) and Mrk 501 (dash-dotted lines), computed for different source emission regions R_{em} , where R_S denotes the Schwarzschild radius of the central SMBH.

5 CTAO simulated observations

The Cherenkov Telescope Array Observatory (CTAO) is a next-generation ground-based observatory designed to explore the VHE gamma-ray sky with unprecedented sensitivity

and angular resolution. With its broad energy coverage from 20 GeV to beyond 300 TeV, CTAO will investigate extreme astrophysical phenomena including PeVatrons, supernova remnants, and relativistic jets in active galactic nuclei [65]. The observatory’s improved energy resolution and low energy threshold will enable landmark studies of indirect dark matter signatures. These include searches for gamma-ray lines from DM annihilation or decay in the Galactic Center, dwarf spheroidal galaxies and galaxy clusters, as well as broadband emission from TeV-scale WIMP’s (Weakly Interacting Massive Particles) [66–68]. Furthermore, CTAO’s large effective area and ability to resolve spectral cutoffs will also test DM particle models beyond the standard WIMP paradigm, such as dark photons and axion-like particles [69–71].

This section details our simulation framework for spectral analysis of the three target sources, using publicly available instrument response functions (IRFs) from the CTA Prod5 dataset. Our analysis pipeline is implemented with GAMMAPY version 1.3 [72, 73], and includes data simulation, instrument response modeling, and spectral extraction for each source.

5.1 Crab Nebula spectral simulations

Simulated observations of the Crab Nebula were performed using the Southern array layout of the CTAO Alpha Configuration, consisting of 14 Medium-Sized Telescopes (MSTs) and 37 Small-Sized Telescopes (SSTs). We used the instrument response functions (IRFs) from the Prod5 dataset, corresponding to the “South-20deg-AverageAz” configuration, optimised for 50 hours of observation time [74], which include the effective area, energy dispersion, and point spread function. A wobble observation strategy was adopted, with four offset pointings located 0.4° from the target position, at position angles of 0° , 90° , 180° , and 270° .

The total simulated livetime of 200 hours was evenly distributed across these wobble positions. This exposure reflects the role of the Crab Nebula as a standard candle and calibration source in very-high-energy gamma-ray astronomy, for which accumulated observation times of this order are realistic within the CTAO lifetime. The adopted exposure is intended to provide a representative benchmark scenario rather than an optimized observing strategy.

The simulation covered a reconstructed energy range from 0.05 to 200 TeV, with 20 bins per decade, and a true energy range from 0.025 to 300 TeV, with 40 bins per decade, in order to accurately model the instrument response functions and account for IRF tails. A safe energy threshold was defined using GAMMAPY’s `SafeMaskMaker` with the `edisp-bias` method, retaining only energy bins where the energy-dispersion bias, as derived from the instrument response functions (IRFs), is below 10%. This defines a safe reconstructed-energy range consistent with CTAO real-data analyses, ensuring reliable flux reconstruction and limiting systematic effects from the energy dispersion. An ON–OFF technique was used, with background estimation performed using the reflected region method, employing ten reflected OFF regions for improved statistical reliability.

The Crab Nebula’s VHE emission was modeled as a point source centered at the coordinates shown in Table 1, with a log-parabolic spectral energy distribution (Eq. 4.1),

using the parameters detailed in Section 4.1. The resulting simulated differential flux points, extracted across 25 logarithmically spaced energy bins, are shown in Figure 4, as well as the assumed SED model, with and without DPDM attenuation.

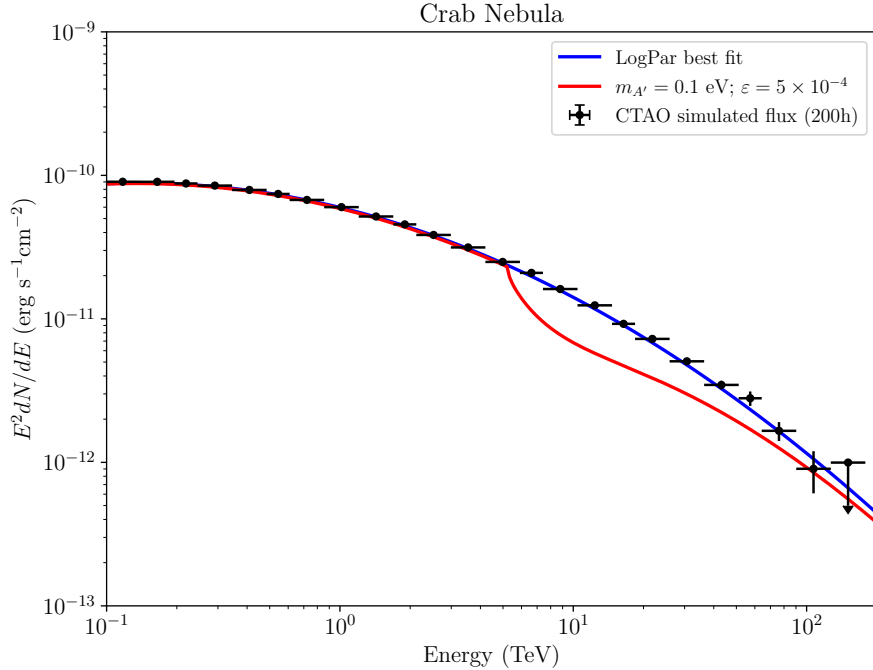


Figure 4. The black points show one simulated CTAO flux realization for the Crab Nebula as $E^2 dN/dE$ across 25 logarithmically-spaced energy bins. The blue line represents the best-fit log-parabola (H_0), while the red line illustrates the dark photon scattering attenuation effect for $m_{A'} = 0.1$ eV and $\varepsilon = 5 \times 10^{-4}$. The best-fit parameters for the null hypothesis are shown in Table 3.

5.2 Mrk 421 and Mrk 501 spectral simulations

Simulated observations of the blazars Mrk 421 and Mrk 501 were performed using the Northern array layout of the CTAO Alpha Configuration, consisting of 4 Large-Sized Telescopes (LSTs) and 9 Medium-Sized Telescopes (MSTs). The instrument response functions (IRFs) were taken from the Prod5 dataset, corresponding to the “North-20deg-AverageAz” configuration¹, optimised for 50 hours of observation time [74]. The same wobble observation strategy used for the Crab Nebula was adopted.

For each blazar, we assume a total simulated livetime of 100 hours, equally distributed across the wobble positions. This exposure is intended to represent a realistic dedicated observing campaign for bright variable blazars. Although such observation

¹The IRFs employed in this analysis correspond to a zenith angle of 20° . The effect of adopting larger zenith angles for the Northern array was assessed separately and found not to significantly modify the derived dark photon constraints within the mass range considered in this work.

times exceed those foreseen for the early CTAO phases, comparable cumulative exposures are expected to be achieved as the observatory approaches its full operational configuration. Moreover, adopting 100 hours per source enables meaningful comparison with previous VHE studies and commonly adopted sensitivity references in the literature.

The reconstructed energy range spanned from 0.05 to 50 TeV, with 20 bins per decade, while the true energy extended from 0.025 to 100 TeV, sampled using 40 bins per decade to ensure proper resolution of instrument response effects. The same safe-energy selection based on the 10% energy-dispersion bias criterion described in Section 5.1 was applied to the blazar datasets. The analysis followed the ON–OFF approach, using the reflected region method for background estimation with ten reflected OFF regions.

Mrk 421 and Mrk 501 were modeled as point sources centered at the coordinates shown in Table 1, with ECPL spectra (Eq. 4.2), using the spectral parameters described in Section 4.2, and incorporating attenuation from the extragalactic background light (EBL) using the model of Domínguez et al. [75]. The resulting simulated differential flux points are shown in Figures 5 and 6.

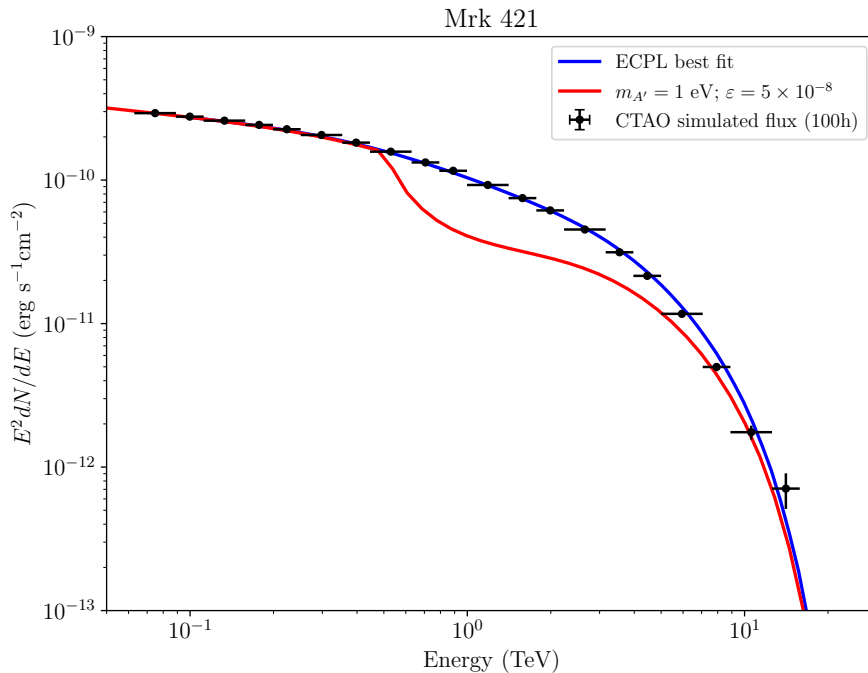


Figure 5. The black points show one simulated CTAO flux realization for Mrk 421 as $E^2 dN/dE$ across 25 logarithmically-spaced energy bins. The blue line represents the best-fit ECPL function (H_0), while the red line illustrates the dark photon scattering attenuation effect for $m_{A'} = 1$ eV and $\varepsilon = 5 \times 10^{-8}$. The best-fit parameters for the null hypothesis are shown in Table 3.

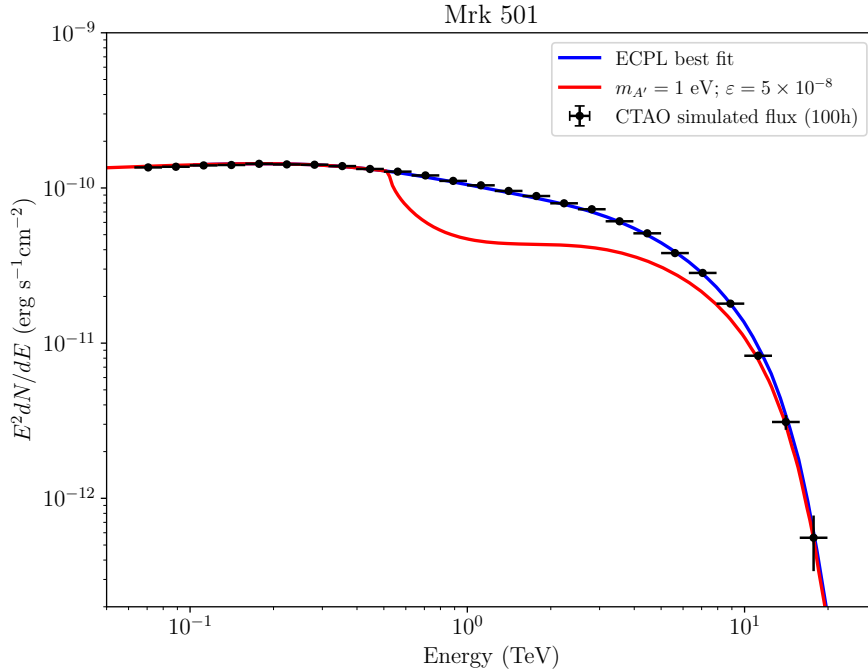


Figure 6. The black points show one simulated CTAO flux realization for Mrk 501 as $E^2 dN/dE$ across 25 logarithmically-spaced energy bins. The blue line represents the best-fit ECPL function (H_0), while the red line illustrates the dark photon scattering attenuation effect for $m_{A'} = 1$ eV and $\epsilon = 5 \times 10^{-8}$. The best-fit parameters for the null hypothesis are shown in Table 3.

6 Model fitting

In this section, we describe the procedure adopted to determine the best-fit parameters of the spectral models and to derive 95% confidence level upper limits on the DPDM kinetic mixing parameter ϵ using a likelihood-based statistical approach.

6.1 Null Hypothesis H_0

For the null hypothesis H_0 , we consider the scenario in which the gamma-ray flux is fully explained by standard astrophysical processes at the source, such as particle acceleration and diffusion. This model defines the intrinsic spectrum of the sources, $\left. \frac{dN}{dE} \right|_{\text{int}}$, as described in Sections 4.1 and 4.2 for the Crab Nebula and the blazars, respectively. As such, H_0 defines the underlying physical scenario in the absence of photon-dark photon interactions and is used to generate the simulated datasets employed in the Monte Carlo realizations.

Strictly, attenuation effects due to the propagation of TeV gamma rays in the MW and IGM must also be encompassed in the null hypothesis, in the form of an energy-dependent attenuation term $f_{\text{att}}(E)$, resulting in the spectral model

$$\left. \frac{dN}{dE} \right|_{H_0} = \left. \frac{dN}{dE} \right|_{\text{int}} \times f_{\text{att}}(E). \quad (6.1)$$

For the Crab Nebula, the effects due to Galactic propagation (e.g., γ - γ interactions with the interstellar radiation field (ISRF) or cosmic microwave background (CMB)) are typically negligible below ~ 100 TeV [76, 77], therefore we assume $f_{\text{att}}(E) \approx 1$.

For Mrk 421 and Mrk 501, the attenuation caused by interactions with the EBL is dominant over the galactic attenuation, and we consider $f_{\text{att}}(E) = f_{\text{EBL}}(E)$. While numerous EBL models exist in the literature [75, 78–81], we use the Dominguez et al. model [75] as our baseline. Varying the EBL model has negligible impact in the constraints [82].

6.2 Alternative Hypothesis H_1

The alternative hypothesis H_1 extends the baseline spectral model by including the photon survival probability induced by photon-dark photon scattering, given by Eq. 2.5. The resulting spectral model is

$$\left. \frac{dN}{dE} \right|_{H_1} = P_{\text{sur}}(m_{A'}, \varepsilon) \times \left. \frac{dN}{dE} \right|_{\text{int}} \times f_{\text{att}}(E), \quad (6.2)$$

where the dependence on the dark photon parameters $m_{A'}$ and ε arises from the scattering cross-section (Eq. 2.4).

6.3 Log-likelihood statistical test

To derive constraints on the DPDM parameters, we adopt a profile-likelihood ratio approach based on the Likelihood Ratio Test (LRT) framework. We use the W-statistic (WStat) [83], as implemented in GAMMAPY [72], which is derived from the Poisson likelihood for on-off measurements, and incorporates systematic uncertainties from background estimation. The WStat fit statistic per energy bin is given by [72]

$$W = 2(\mu_{\text{sig}} + (1 + 1/\alpha)\mu_{\text{bkg}} - n_{\text{on}} \log(\mu_{\text{sig}} + \mu_{\text{bkg}}) - n_{\text{off}} \log(\mu_{\text{bkg}}/\alpha)), \quad (6.3)$$

where n_{on} and n_{off} are the observed counts in the on and off regions, μ_{sig} is the expected number of signal counts in the on region, and α is the exposure ratio between the on and off regions.

Upper limits on the kinetic mixing parameter are derived using the profile-likelihood test statistic

$$TS(m_{A'}; \varepsilon) = W_{H_1}(m_{A'}; \varepsilon) - W_{H_1}(m_{A'}; \hat{\varepsilon}), \quad (6.4)$$

where $\hat{\varepsilon}$ is the value of the mixing parameter that minimizes the WStat under the alternative hypothesis.

In the asymptotic regime, the test statistic is expected to follow a χ^2 distribution with one degree of freedom, according to Wilks' theorem. Under this assumption, a value of $TS = 2.71$ corresponds to a one-sided 95% confidence level upper limit on ε .

When fitting the Crab Nebula data, the spectral parameters (N_0, α, β) and the background normalization were left free to vary. For the DPDM contribution, we varied the mixing parameter ε while keeping the dark photon mass $m_{A'}$ fixed at each evaluation point. The same fitting procedure was applied to Mrk 421 and Mrk 501, whose free spectral parameters were $(N_0, \alpha, E_{\text{cut}})$.

7 Results

Figures 7, 8, and 9 show the expected 95% confidence level upper limits on the kinetic mixing parameter ε as a function of the DPDM mass $m_{A'}$, obtained for the Crab Nebula, Mrk 421, and Mrk 501, respectively. In each case, the solid line shows the median expected upper limit, and the shaded bands represent the corresponding 68% and 95% containment intervals obtained from 100 independent Poisson realizations of the simulated observations.

In the case of the blazars, the emission is assumed to be located at $R_{\text{em}} = 4R_S$. The parameters of the best-fit spectral models used in the likelihood analysis are listed in Table 3. These were obtained by fitting the simulated spectra under the null hypothesis, i.e., assuming no attenuation from photon-dark photon scattering, and define the reference intrinsic spectral models used in the subsequent likelihood scans over the DPDM mixing parameter.

Numerically, the most stringent upper limits were obtained for the blazars Mrk 421 and Mrk 501, where values as low as $\varepsilon \sim 10^{-8}$ could be constrained at the 95% confidence level for dark photon masses around $m_{A'} \sim 0.1\text{--}1$ eV. For the Crab Nebula, which lies within the Milky Way halo and does not benefit from a central dark matter spike, the limits are comparatively weaker, constraining values of $\varepsilon \gtrsim 2 \times 10^{-4}$ in the $m_{A'} \sim 0.01\text{--}0.1$ eV mass range.

Since the analysis assumes specific dark matter distributions for each system, it is important to highlight the astrophysical uncertainties that affect the results. In particular, for Mrk 421 and Mrk 501, the presence of a dark matter spike around the central supermassive black hole plays a critical role in enhancing the optical depth to photon-dark photon scattering. However, the formation and long-term stability of such spikes are still debated, as they can be disrupted by black hole mergers or dynamical heating processes [24, 85]. Figure 10 illustrates the impact on the constraints when the central dark matter spike is omitted and a canonical NFW profile is adopted, with r_s and ρ_s set to the same values as in the corresponding spiked profile scenario.

The variation of the emission region's location relative to the black hole also impacts the total traversed dark matter density, as shown in Figure 3. The resulting constraints on ε for Mrk 501, evaluated at different values of R_{em} , are presented in Figure 11. As expected, when the emission region is located far from the center, such that it lies partially or entirely outside the high-density region associated with the spike, the effective optical depth decreases. In these cases, the resulting constraints become comparable to those obtained under a canonical NFW profile without a spike.

Figure 12 presents a combined view of the constraints derived from the three sources considered in this work, also showing the constraints from the CAST experiment [18] and

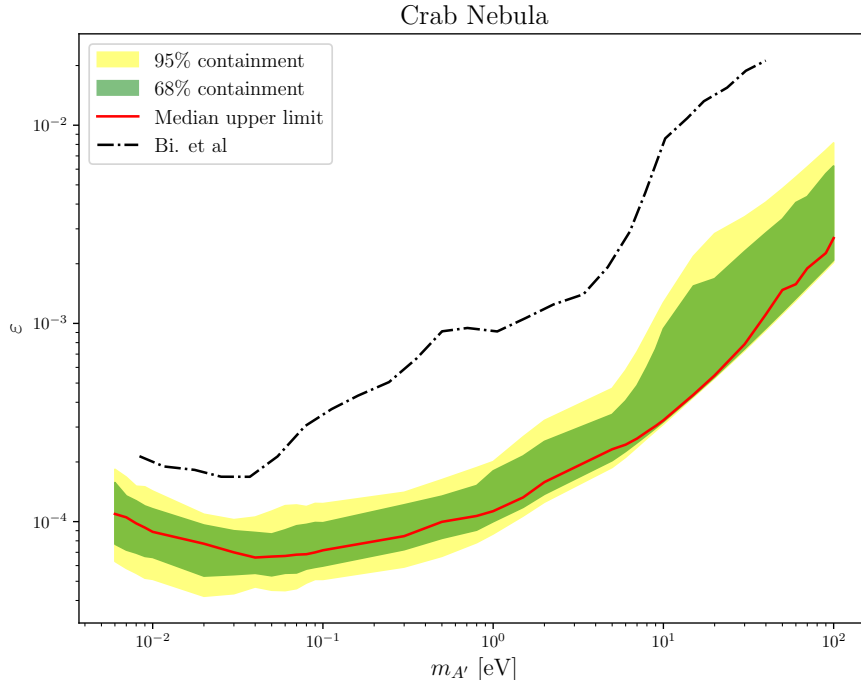


Figure 7. Expected 95% confidence level upper limits on the kinetic mixing parameter ε derived from simulated CTAO observations of the Crab Nebula. The solid red line shows the median expected upper limit, while the shaded regions indicate the 68% and 95% containment bands around the median. Constraints from Ref. [21] (dash-dotted lines) are shown for comparison.

from solar cooling rates [84]. The constraints obtained with CTAO simulations for the blazars approach the sensitivity of CAST in the mass range $m_{A'} \sim 0.1\text{--}1$ eV, but remain significantly weaker than those derived from solar physics. Nevertheless, the constraints derived in this work are complementary to those from CAST and solar energy loss. While the latter probe photon–dark photon mixing in laboratory settings and stellar interiors, respectively, our analysis targets a distinct physical regime, providing an independent and high-energy test of the DPDM scenario.

Source	N_0 ($\text{TeV}^{-1}\text{cm}^{-2}\text{s}^{-1}$)	α	β	E_{cut} (TeV)
Crab Nebula	$(2.41 \pm 0.09) \times 10^{-13}$	2.79 ± 0.02	$(1.00 \pm 0.04) \times 10^{-1}$	—
Mrk 421	$(1.16 \pm 0.02) \times 10^{-10}$	2.18 ± 0.01	—	3.61 ± 0.13
Mrk 501	$(1.10 \pm 0.01) \times 10^{-10}$	1.91 ± 0.01	—	5.92 ± 0.19

Table 3. Best-fit parameters of the intrinsic spectral models used to describe the simulated CTAO observations for each source. The fits were performed under the null hypothesis, assuming no attenuation from dark photon scattering. A log-parabola spectral shape was adopted for the Crab Nebula, while an exponential cutoff power-law model was used for Mrk 421 and Mrk 501.

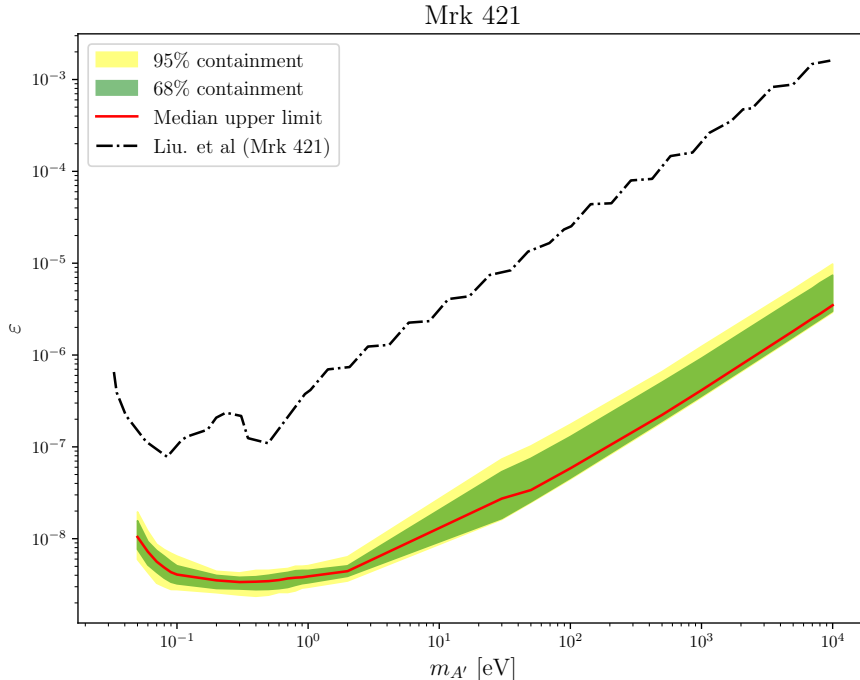


Figure 8. Expected 95% confidence level upper limits on the kinetic mixing parameter ε derived from simulated CTAO observations of Mrk 421. The solid red line shows the median expected upper limit, while the shaded regions indicate the 68% and 95% containment bands around the median. Constraints from Ref. [82] (dash-dotted lines) are shown for comparison.

8 Conclusion

In this work, we investigated the possibility of probing dark photon dark matter (DPDM) through spectral attenuation effects in very-high-energy (VHE) gamma rays. Using simulated CTAO observations, we derived for the first time its sensitivity to constrain the kinetic mixing parameter ε for a range of DPDM masses.

We considered three representative VHE sources – the Crab Nebula, Mrk 421, and Mrk 501 – and modeled the expected attenuation assuming dark photons make up the entire dark matter content. The resulting constraints depend on the dark matter distribution along the line of sight. In particular, for the blazars Mrk 421 and Mrk 501, the presence of a dark matter spike around the central supermassive black hole significantly enhances the predicted attenuation signal.

Additionally, we explored the dependence of the constraints on the assumed location of the gamma-ray emission region. In compact emission scenarios, the traversed dark matter column density, and hence the optical depth, is substantially increased, leading to stronger constraints on ε .

While the bounds obtained here are not yet as strong as those derived from solar energy loss or laboratory experiments like CAST, they are complementary since our

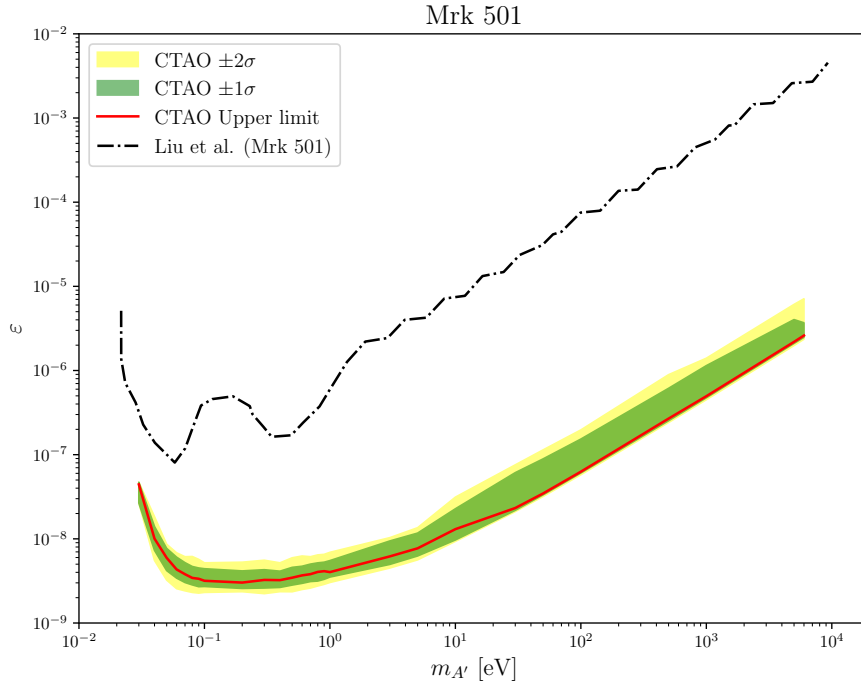


Figure 9. Expected 95% confidence level upper limits on the kinetic mixing parameter ε derived from simulated CTAO observations of Mrk 501. The solid red line shows the median expected upper limit, while the shaded regions indicate the 68% and 95% containment bands around the median. Constraints from Ref. [82] (dash-dotted lines) are shown for comparison.

analysis provides an independent high-energy test of the DPDM scenario. These results illustrate the potential of CTAO to contribute to the broader experimental effort to constrain hidden-sector dark matter models.

Further improvements could be achieved by including a larger sample of VHE sources with diverse spectral shapes and redshifts, as well as by refining the modeling of dark matter distributions through high-resolution simulations and multi-wavelength observations. In addition, applying this analysis to real CTAO data in the future, once available, will allow for tests of these scenarios under more realistic observational conditions.

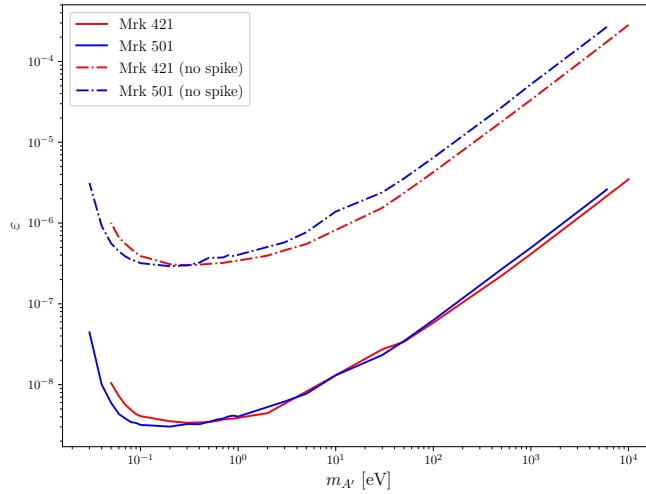


Figure 10. Expected 95% confidence level upper limits on the kinetic mixing parameter ε derived from simulated CTAO observations of Mrk 421 and Mrk 501. Solid lines correspond to scenarios including a central dark matter spike, assuming an emission region located at $R_{\text{em}} = 4R_S$. Dash-dotted lines show the results obtained under a canonical NFW profile with scale parameters ρ_s and r_s as given in Table 2, also assuming $R_{\text{em}} = 4R_S$.

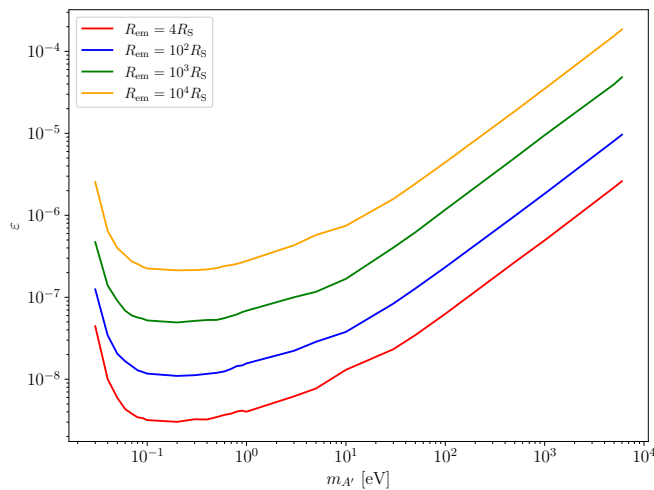


Figure 11. Expected 95% confidence level upper limits on the kinetic mixing parameter ε derived from simulated CTAO observations of Mrk 501 for different emission regions R_{em} .

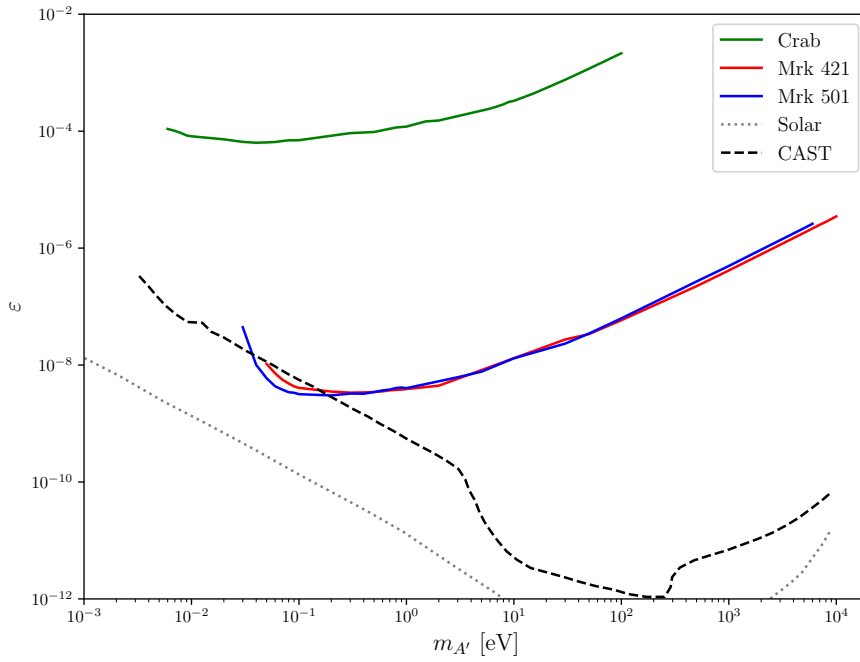


Figure 12. Constraints on the kinetic mixing parameter ε derived from simulated CTAO observations of the Crab Nebula (green), Mrk 421 (red), and Mrk 501 (blue), represented as solid lines (this work). Existing bounds from solar energy loss (gray dotted line) [84] and from the CAST helioscope experiment (black dashed line) [18] are included for comparison.

Acknowledgments

This research has made use of the CTA instrument response functions provided by the CTA Consortium and Observatory, see <https://www.ctao.org/for-scientists/performance/> (version prod5 v0.1; [74]) for more details.

The authors are supported by the São Paulo Research Foundation (FAPESP) through grant number 2021/01089-1. VdS is supported by CNPq through grant number 308837/2023-1. JGM is supported by FAPESP through grant number 2022/16842-0. The authors acknowledge the National Laboratory for Scientific Computing (LNCC/MCTI, Brazil) for providing HPC resources for the SDumont supercomputer (<http://sdumont.lncc.br>).

References

- [1] PLANCK collaboration, *Planck 2018 results. VI. Cosmological parameters*, *Astron. Astrophys.* **641** (2020) A6 [[1807.06209](#)].
- [2] M. Persic, P. Salucci and F. Stel, *The Universal rotation curve of spiral galaxies: 1. The Dark matter connection*, *Mon. Not. Roy. Astron. Soc.* **281** (1996) 27 [[astro-ph/9506004](#)].
- [3] V.C. Rubin and W.K. Ford, Jr., *Rotation of the Andromeda Nebula from a Spectroscopic Survey of Emission Regions*, *Astrophysical Journal* **159** (1970) 379.
- [4] D. Clowe, M. Bradac, A.H. Gonzalez, M. Markevitch, S.W. Randall, C. Jones et al., *A direct empirical proof of the existence of dark matter*, *Astrophys. J. Lett.* **648** (2006) L109 [[astro-ph/0608407](#)].
- [5] PLANCK collaboration, *Planck 2018 results. X. Constraints on inflation*, *Astron. Astrophys.* **641** (2020) A10 [[1807.06211](#)].
- [6] SDSS collaboration, *Detection of the Baryon Acoustic Peak in the Large-Scale Correlation Function of SDSS Luminous Red Galaxies*, *Astrophys. J.* **633** (2005) 560 [[astro-ph/0501171](#)].
- [7] LUX collaboration, *Limits on spin-dependent WIMP-nucleon cross section obtained from the complete LUX exposure*, *Phys. Rev. Lett.* **118** (2017) 251302 [[1705.03380](#)].
- [8] XENON collaboration, *First Dark Matter Search with Nuclear Recoils from the XENONnT Experiment*, *Phys. Rev. Lett.* **131** (2023) 041003 [[2303.14729](#)].
- [9] PANDAX collaboration, *Search for Solar B8 Neutrinos in the PandaX-4T Experiment Using Neutrino-Nucleus Coherent Scattering*, *Phys. Rev. Lett.* **130** (2023) 021802 [[2207.04883](#)].
- [10] FERMI-LAT collaboration, *Searching for Dark Matter Annihilation from Milky Way Dwarf Spheroidal Galaxies with Six Years of Fermi Large Area Telescope Data*, *Phys. Rev. Lett.* **115** (2015) 231301 [[1503.02641](#)].
- [11] H.E.S.S. collaboration, *Search for Photon-Linelike Signatures from Dark Matter Annihilations with H.E.S.S.*, *Phys. Rev. Lett.* **110** (2013) 041301 [[1301.1173](#)].
- [12] ICECUBE collaboration, *Search for neutrino lines from dark matter annihilation and decay with IceCube*, *Phys. Rev. D* **108** (2023) 102004 [[2303.13663](#)].
- [13] M. Cirelli, A. Strumia and J. Zupan, *Dark Matter*, [2406.01705](#).

- [14] B. Holdom, *Two $u(1)$'s and ϵ charge shifts*, *Physics Letters B* **166** (1986) 196.
- [15] P. Fayet, *Extra $u(1)$'s and new forces*, *Nuclear Physics B* **347** (1990) 743.
- [16] A.E. Nelson and J. Scholtz, *Dark light, dark matter, and the misalignment mechanism*, *Phys. Rev. D* **84** (2011) 103501.
- [17] P. Arias, D. Cadamuro, M. Goodsell, J. Jaeckel, J. Redondo and A. Ringwald, *Wispy cold dark matter*, *Journal of Cosmology and Astroparticle Physics* **2012** (2012) 013.
- [18] J. Redondo, *Helioscope Bounds on Hidden Sector Photons*, *JCAP* **07** (2008) 008 [[0801.1527](#)].
- [19] M. Fabbrichesi, E. Gabrielli and G. Lanfranchi, *The Dark Photon*, **2005.01515**.
- [20] J.L. Bernal, A. Caputo, G. Sato-Polito, J. Mirocha and M. Kamionkowski, *Seeking dark matter with γ -ray attenuation*, *Phys. Rev. D* **107** (2023) 103046 [[2208.13794](#)].
- [21] X. Bi, Y. Gao, J. Guo, N. Houston, T. Li, F. Xu et al., *Axion and dark photon limits from crab nebula high-energy gamma rays*, *Phys. Rev. D* **103** (2021) 043018.
- [22] H. Zhao, *Analytical models for galactic nuclei*, *Mon. Not. Roy. Astron. Soc.* **278** (1996) 488 [[astro-ph/9509122](#)].
- [23] J.F. Navarro, C.S. Frenk and S.D.M. White, *A Universal density profile from hierarchical clustering*, *Astrophys. J.* **490** (1997) 493 [[astro-ph/9611107](#)].
- [24] P. Gondolo and J. Silk, *Dark matter annihilation at the galactic center*, *Phys. Rev. Lett.* **83** (1999) 1719 [[astro-ph/9906391](#)].
- [25] G.D. Quinlan, L. Hernquist and S. Sigurdsson, *Models of Galaxies with Central Black Holes: Adiabatic Growth in Spherical Galaxies*, *Astrophys. J.* **440** (1995) 554 [[astro-ph/9407005](#)].
- [26] N. Neumayer, *The supermassive black hole at the heart of centaurus a: Revealed by the kinematics of gas and stars*, *Publications of the Astronomical Society of Australia* **27** (2010) 449–456.
- [27] K. Gebhardt and J. Thomas, *The Black Hole Mass, Stellar Mass-to-Light Ratio, and Dark Halo in M87*, *Astrophysical Journal* **700** (2009) 1690 [[0906.1492](#)].
- [28] M. Gorchtein, S. Profumo and L. Ubaldi, *Probing dark matter with active galactic nuclei jets*, *Phys. Rev. D* **82** (2010) 083514.
- [29] J.J. Hester, *The Crab Nebula : an astrophysical chimera.*, *journal = Annual Review of Astronomy and Astrophysics*, **46** (2008) 127.
- [30] R. Bühler and R. Blandford, *The surprising Crab pulsar and its nebula: A review*, *Rept. Prog. Phys.* **77** (2014) 066901 [[1309.7046](#)].
- [31] E. Amato and B. Olmi, *The crab pulsar and nebula as seen in gamma-rays*, *Universe* **07** (2021) 448.
- [32] M.J. Rees and J.E. Gunn, *The origin of the magnetic field and relativistic particles in the crab nebula*, *Monthly Notices of the Royal Astronomical Society* **167** (1974) 1 [<https://academic.oup.com/mnras/article-pdf/167/1/1/8079729/mnras167-0001.pdf>].
- [33] A.M. Atoyan and F.A. Aharonian, *On the mechanisms of gamma radiation in the crab nebula*, *Monthly Notices of the Royal Astronomical Society* **278** (1996) 525 [<https://academic.oup.com/mnras/article-pdf/278/2/525/2793455/278-2-525.pdf>].

- [34] A.M. Hillas, C.W. Akerlof, S.D. Biller, J.H. Buckley, D.A. Carter-Lewis, M. Catanese et al., *The Spectrum of Teravolt Gamma Rays from the Crab Nebula*, *Astrophysical Journal* **503** (1998) 744.
- [35] M. Meyer, D. Horns and H.S. Zechlin, *The Crab Nebula as a standard candle in very high-energy astrophysics*, *Astronomy & Astrophysics* **523** (2010) A2 [1008.4524].
- [36] H.E.S.S. collaboration, *Spectrum and extension of the inverse-Compton emission of the Crab Nebula from a combined Fermi-LAT and H.E.S.S. analysis*, *Astron. Astrophys.* **686** (2024) A308 [2403.12608].
- [37] Lhaaso Collaboration, Z. Cao, F. Aharonian, Q. An, Axikegu, L.X. Bai et al., *Peta-electron volt gamma-ray emission from the Crab Nebula*, *Science* **373** (2021) 425 [2111.06545].
- [38] Q.-Y. Peng, B.-W. Bao, F.-W. Lu and L. Zhang, *Multiband emission up to pev energy from the crab nebula in a spatially dependent lepto-hadronic model*, *The Astrophysical Journal* **926** (2022) 7.
- [39] L. Nie, Y. Liu, Z. Jiang and X. Geng, *Ultra-high-energy Gamma-Ray Radiation from the Crab Pulsar Wind Nebula*, *Astrophys. J.* **924** (2022) 42 [2201.03796].
- [40] HAWC collaboration, *Measurement of the Crab Nebula at the Highest Energies with HAWC*, *Astrophys. J.* **881** (2019) 134 [1905.12518].
- [41] G. Ghisellini, F. Tavecchio, L. Foschini, G. Ghirlanda, L. Maraschi and A. Celotti, *General physical properties of bright fermi blazars: Properties of bright fermi blazars*, *Monthly Notices of the Royal Astronomical Society* **402** (2009) 497–518.
- [42] J.A. Gaidos, C.W. Akerlof, S. Biller, P.J. Boyle, A.C. Breslin, J.H. Buckley et al., *Extremely rapid bursts of TeV photons from the active galaxy Markarian 421*, *Nature* **383** (1996) 319.
- [43] M. Punch, C.W. Akerlof, M.F. Cawley, M. Chantell, D.J. Fegan, S. Fennell et al., *Detection of TeV photons from the active galaxy Markarian 421*, *Nature* **358** (1992) 477.
- [44] F. Krennrich, I.H. Bond, S.M. Bradbury, J.H. Buckley, D.A. Carter-Lewis, W. Cui et al., *Discovery of spectral variability of markarian 421 at tev energies*, *The Astrophysical Journal* **575** (2002) L9.
- [45] Aharonian, F., Akhperjanian, A., Beilicke, M., Bernlöhr, K., Börst, H., Bojahr, H. et al., *Variations of the tev energy spectrum at different flux levels of mkn 421 observed with the hegra system of cherenkov telescopes*, *A&A* **393** (2002) 89.
- [46] J. Quinn, C.W. Akerlof, S. Biller, J. Buckley, D.A. Carter-Lewis, M.F. Cawley et al., *Detection of gamma rays with e > 300 gev from markarian 501*, *The Astrophysical Journal* **456** (1996) L83.
- [47] HEGRA collaboration, *The temporal characteristics of the TeV gamma emission from mkn 501 in 1997 - part. 2. Results from hegra ct1 and ct2*, *Astron. Astrophys.* **349** (1999) 29 [astro-ph/9901284].
- [48] J. Albert, E. Aliu, H. Anderhub, P. Antoranz, A. Armada, M. Asensio et al., *Observations of markarian 421 with the magic telescope*, *The Astrophysical Journal* **663** (2007) 125.
- [49] Aharonian, F. A., Akhperjanian, A. G., Barrio, J. A., Bernlöhr, K., Bolz, O., Börst, H. et al., *Reanalysis of the high energy cutoff of the 1997 mkn 501 tev energy spectrum*, *A&A* **366** (2001) 62.

- [50] F. Aharonian, A.G. Akhperjanian, G. Anton, U. Barres de Almeida, A.R. Bazer-Bachi, Y. Becherini et al., *Simultaneous multiwavelength observations of the second exceptional γ -ray flare of pks 2155–304 in july 2006*, *Astronomy & Astrophysics* **502** (2009) 749–770.
- [51] A.A. Abdo, M. Ackermann, M. Ajello, L. Baldini, J. Ballet, G. Barbiellini et al., *Fermi large area telescope observations of markarian 421: The missing piece of its spectral energy distribution*, *The Astrophysical Journal* **736** (2011) 131.
- [52] A. Albert et al., *Long-term Spectra of the Blazars Mrk 421 and Mrk 501 at TeV Energies Seen by HAWC*, *Astrophys. J.* **929** (2022) 125 [2106.03946].
- [53] V.A. Acciari, E. Aliu, T. Arlen, T. Aune, M. Beilicke, W. Benbow et al., *TeV and multi-wavelength observations of mrk 421 in 2006–2008*, *The Astrophysical Journal* **738** (2011) 25.
- [54] V.A. Acciari, T. Arlen, T. Aune, M. Beilicke, W. Benbow, M. Böttcher et al., *Spectral energy distribution of markarian 501: Quiescent state versus extreme outburst*, *The Astrophysical Journal* **729** (2011) 2.
- [55] HEGRA collaboration, *The time averaged TeV energy spectrum of mkn 501 of the extraordinary 1997 outburst as measured with the stereoscopic Cherenkov telescope system of hegra*, *Astron. Astrophys.* **349** (1999) 11 [astro-ph/9903386].
- [56] D. Coe, *Dark Matter Halo Mass Profiles*, *arXiv e-prints* (2010) arXiv:1005.0411 [1005.0411].
- [57] G. Tormen, F.R. Bouchet and S.D.M. White, *The Structure and dynamical evolution of dark matter halos*, *Mon. Not. Roy. Astron. Soc.* **286** (1997) 865 [astro-ph/9603132].
- [58] E. Corbelli, S. Lorenzoni, R. Waltherbos, R. Braun and D. Thilker, *A wide-field H I mosaic of Messier 31. II. The disk warp, rotation, and the dark matter halo*, *Astronomy & Astrophysics* **511** (2010) A89 [0912.4133].
- [59] T. Lacroix, M. Karami, A.E. Broderick, J. Silk and C. Boehm, *Unique probe of dark matter in the core of M87 with the Event Horizon Telescope*, *Phys. Rev. D* **96** (2017) 063008 [1611.01961].
- [60] S.P. Wakely and D. Horan, *TeVCat: An online catalog for Very High Energy Gamma-Ray Astronomy*, *International Cosmic Ray Conference* **3** (2008) 1341.
- [61] R. Falomo, J.K. Kotilainen and A. Treves, *The Black Hole Mass of BL Lacertae Objects from the Stellar Velocity Dispersion of the Host Galaxy*, *Astrophysical Journal Letters* **569** (2002) L35 [astro-ph/0203199].
- [62] M.G. Blasi et al., *The TeV blazar Markarian 421 at the highest spatial resolution*, *Astron. Astrophys.* **559** (2013) A75 [1310.4973].
- [63] A.A. Abdo, M. Ackermann, M. Ajello, A. Allafort, L. Baldini, J. Ballet et al., *Insights into the high-energy γ -ray emission of markarian 501 from extensive multifrequency observations in the fermi era*, *The Astrophysical Journal* **727** (2011) 129.
- [64] L. Liu, Y. Jiang, J. Deng, Z. Chen and C. Ma, *Unveiling the Emission and Variation Mechanism of Mrk 501: Using the Multi-Wavelength Data at Different Time Scale*, *Universe* **10** (2024) 114.
- [65] T.C. Consortium, *Science with the cherenkov telescope array*, *World Scientific* (2019) .

- [66] A. Viana, H. Schoorlemmer, A. Albert, V. de Souza, J.P. Harding and J. Hinton, *Searching for Dark Matter in the Galactic Halo with a Wide Field of View TeV Gamma-ray Observatory in the Southern Hemisphere*, *JCAP* **12** (2019) 061 [[1906.03353](#)].
- [67] CTAO collaboration, *Dark matter line searches with the Cherenkov Telescope Array*, *JCAP* **07** (2024) 047 [[2403.04857](#)].
- [68] C. Duangchan et al., *CTA sensitivity on TeV scale dark matter models with complementary limits from direct detection*, *JCAP* **05** (2022) 038 [[2202.07321](#)].
- [69] Y.-F. Liang, C. Zhang, Z.-Q. Xia, L. Feng, Q. Yuan and Y.-Z. Fan, *Constraints on axion-like particle properties with TeV gamma-ray observations of Galactic sources*, *JCAP* **06** (2019) 042 [[1804.07186](#)].
- [70] I. Reis, E. Moulin, A. Viana and V.P. Goncalves, *Sensitivity to sub-GeV dark matter from cosmic-ray scattering with very-high-energy gamma-ray observatories*, *JCAP* **07** (2024) 012 [[2403.09343](#)].
- [71] T. Linden, T.T.Q. Nguyen and T.M.P. Tait, *Indirect searches for dark photon-photon tridents in celestial objects*, 2024.
- [72] A. Donath, R. Terrier, Q. Remy, A. Sinha, C. Nigro, F. Pintore et al., *Gammapy: A python package for gamma-ray astronomy*, *A&A* **678** (2023) A157.
- [73] F. Acero, A. Aguasca-Cabot, J. Bernete, N. Biederbeck, J. Djuvsland, A. Donath et al., *Gammapy: Python toolbox for gamma-ray astronomy*, Jan., 2025. [10.5281/zenodo.14760974](#).
- [74] C.T.A. Observatory and C.T.A. Consortium, *CTAO Instrument Response Functions - prod5 version v0.1*, 2021. [10.5281/zenodo.5499840](#).
- [75] A. Dominguez, J.R. Primack, D. Rosario, F. Prada, R. Gilmore, S.M. Faber et al., *Extragalactic Background Light Inferred from AEGIS Galaxy SED-type Fractions*, in *25th Texas Symposium on Relativistic Astrophysics*, F.M. Rieger, C. van Eldik and W. Hofmann, eds., p. 228, Jan., 2010, DOI [[1103.4534](#)].
- [76] Z. Cao, F.A. Aharonian, Q. An, B. Axikegu, L. X., Y.X. Bai, Y.W. Bao et al., *Ultrahigh-energy photons up to 1.4 petaelectronvolts from 12 γ -ray Galactic sources*, *Nature* **594** (2021) 33.
- [77] I.V. Moskalenko, T.A. Porter and A.W. Strong, *Attenuation of the gamma rays by the milky way interstellar radiation field*, *Astrophys. J. Lett.* **640** (2006) L155 [[astro-ph/0511149](#)].
- [78] A. Franceschini, G. Rodighiero and M. Vaccari, *Extragalactic optical-infrared background radiation, its time evolution and the cosmic photon-photon opacity*, *Astronomy & Astrophysics* **487** (2008) 837 [[0805.1841](#)].
- [79] J.D. Finke, S. Razzaque and C.D. Dermer, *Modeling the Extragalactic Background Light from Stars and Dust*, *Astrophysical Journal* **712** (2010) 238 [[0905.1115](#)].
- [80] A. Franceschini and G. Rodighiero, *The extragalactic background light revisited and the cosmic photon-photon opacity*, *Astron. Astrophys.* **603** (2017) A34 [[1705.10256](#)].
- [81] A. Saldana-Lopez, A. Domínguez, P.G. Pérez-González, J. Finke, M. Ajello, J.R. Primack et al., *An observational determination of the evolving extragalactic background light from the multiwavelength HST/CANDELS survey in the Fermi and CTA era*, *Mon. Not. Roy. Astron. Soc.* **507** (2021) 5144 [[2012.03035](#)].

- [82] T. Liu, M. Lu and X. Hu, *Constraining dark photon parameters based on the very high energy observations of blazars*, *The European Physical Journal C* **84** (2024) 723.
- [83] W. Cash, *Parameter estimation in astronomy through application of the likelihood ratio.*, *Astrophysical Journal* **228** (1979) 939.
- [84] H. An, M. Pospelov and J. Pradler, *New stellar constraints on dark photons*, *Physics Letters B* **725** (2013) 190.
- [85] D. Merritt, *Evolution of the dark matter distribution at the galactic center*, *Phys. Rev. Lett.* **92** (2004) 201304.